J. Fluid Mech. (2017), *vol.* 814, *pp.* 69–94. © Cambridge University Press 2017
doi:10.1017/jfm.2017.21

Influence of slip on the three-dimensional instability of flow past an elongated superhydrophobic bluff body

Y. L. Xiong[1] **and D. Yang**[2,†]

[1]Department of Mechanics, Huazhong University of Science and Technology, Wuhan 430074, China

[2]School of Naval Architecture and Ocean Engineering, Huazhong University of Science and Technology, Wuhan 430074, China

(Received 24 December 2015; revised 19 December 2016; accepted 19 December 2016; first published online 2 February 2017)

The effects of superhydrophobic surfaces (SHSs), which consist of microgrates oriented transverse to the flow direction, on the onset of three-dimensional instability of flow past a bluff body were studied using Floquet analysis. The SHS was modelled on an air–water interface with a shear-free condition. The results showed that SHSs increased the vortex shedding frequency. Floquet analysis revealed that modes B′ and S′ were suppressed dramatically by the partial-slip condition compared with a regular no-slip body; however, mode A was less affected. Correspondingly, the critical spanwise wavelengths were not significantly affected by SHSs. A similar phenomenon was observed in flow past a circular cylinder coated by SHSs. The results also revealed that modes B′ and S′ were collapsed into mode A due to the increased width of the air–water region for flow past an elongated body. Furthermore, the critical Reynold numbers of different modes were diversely affected by gas fraction (GF) variations. The unstable modes with short wavelengths, such as modes B′ and S′, stabilized with increasing GF. Conversely, the opposite was seen for the unstable mode A with a longer wavelength. The exact critical Reynolds number depended on the geometric configuration, which should be between the critical values of the two extreme cases. The application of SHSs could modify the transition route from two- to three-dimensionality by alternating different unstable modes. As the wavelength of the unstable mode decreases, the inhibition of three-dimensional instability becomes more efficient by SHSs.

Key words: flow control, instability control, vortex shedding

1. Introduction

Flow past a bluff object is a fundamental topic in fluid mechanics, having attracted the attention of researchers for nearly a century (e.g. Roshko 1955; Williamson 1996) in view of its numerous engineering applications. A transition from a steady wake flow field to laminar two-dimensional vortex shedding occurs because of Hopf bifurcation at a low Reynolds number. Further transitions cause the formation

† Email address for correspondence: dan_yang@hust.edu.cn

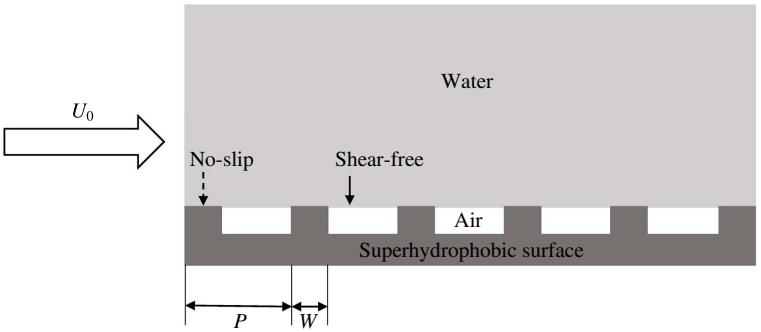

FIGURE 1. Schematic illustration of a superhydrophobic surface with air trapped between the microfeatures. The air–water interface produces shear-free regions.

of three-dimensional vortex structures in the wake and eventually, as the Reynolds number increases, turbulence. Vortex structures cause time-dependent dynamic loads to be exerted on an object, and this may lead to flow-induced vibration, the generation of noise, structural fatigue and turbulent mixing. Several methods of suppressing vortex structures in a bluff-body wake flow have been introduced in recent decades. These control methods involve the addition of energy, such as applying suction to or blowing on the surface of the object (Delaunay & Kaiktsis 2001; Dong, Triantafyllou & Karniadakis 2008), heating the surface (Lecordier, Hamma & Paranthoen 1991) or modifying the geometry of the system such as by fixing a splitter plate (Roshko 1955) or a small object (Mittal & Raghuvanshi 2001; Yildirim, Rindt & Aa 2010) in the wake.

Hydrophobic surfaces and superhydrophobic surfaces (SHSs) (produced through a combination of hydrophobicity and surface roughness at the micro- and/or nanoscale), which produce a composite solid–gas–liquid boundary, have recently begun to be considered important candidates for decreasing drag, improving heat transfer and modifying turbulent structures (Rothstein 2010; Park, Sun & Kim 2014). Hydrophobic surfaces and SHSs are found in nature, e.g. the self-cleaning lotus leaf (Roach, Shirtcliffe & Newton 2008) and the surfaces of the fishing spider (Flynn & Bush 2008). As illustrated in figure 1, an air–water interface forms on such surfaces between the microfeatures, and the trapped gas produces partial-slip conditions. No-slip conditions have been replaced with partial-slip conditions in a number of studies to investigate the effects. Türk *et al.* (2014) performed a series of direct numerical simulations (DNS) using channel flow under alternating no-slip and shear-free conditions. They found that the drag reduction was mainly governed by an effective slip length. For a large spanwise width of the free-slip area, the effective slip length can be significantly reduced because of the underlying turbulence and secondary flow. A similar drag reduction mechanism is also found in the DNS results with more varied superhydrophobic patterns (Rastegari & Akhavan 2015).

In terms of flow past a bluff body, Muralidhar *et al.* (2011) and Daniello *et al.* (2013) studied flow past a superhydrophobic-coated cylinder and found that the shedding frequency increased with slip in the flow direction, and that the flow behaviour was sensitive to the slip direction. Mastrokalos, Papadopoulos & Kaiktsis (2015) found that, for the same non-dimensional slip length, the wake can be stabilized by causing slip conditions to occur on only part of the cylinder surface. SHSs have recently attracted a great deal of attention because they can be broadly

applied to decrease drag and control flow. However, it remains unclear how SHSs affect the three-dimensionality of flow fields. Presently, we seek to investigate how the addition of a partial-slip boundary condition affects three-dimensional transition in the wake of a bluff body.

The onset of three-dimensional instability and the subsequent three-dimensional flow are fundamental to the turbulence found in the wake of a bluff body. Many studies have investigated this issue (Barkley & Henderson 1996; Robichaux, Balachandar & Vanka 1999). It has been proved both numerically and experimentally that there are only two synchronized modes and one quasi-periodic mode in spatio-temporal and spatially symmetrical flows (Marques, Lopez & Blackburn 2004) such as flow past a cylindrical object. Barkley & Henderson (1996) used Floquet stability analysis to investigate the onset of three-dimensional instability in flow past a circular cylinder, and they predicted the existence of modes A and B in such a flow. The critical Reynolds number and the dominant spanwise wavelength they predicted agreed well with the results of experiments previously performed by Williamson (1988). Similar modes A and B were also found in flow past a square cylinder by Robichaux *et al.* (1999). A subharmonic mode C was found experimentally in bluff ring wakes by Zhang *et al.* (1995) and later by Sheard, Thompson & Hourigan (2003). Mode C has also been found in flow past a square cylinder with an angle of incidence (Sheard, Fitzgerald & Ryan 2009), flow around two staggered circular cylinders (Carmo *et al.* 2008) and flow past an inclined flat plate (Yang *et al.* 2013) and an aerofoil (Meneghini *et al.* 2011). Mode C appears when the underlying wake symmetry of a flow is broken. Blackburn & Sheard (2010) examined the relationship between the quasi-periodic mode (mode QP) and mode C, and attempted to determine how mode QP was replaced by mode C by distorting a circular cylinder into a ring and rotating a square cylinder around its axis.

Previous studies showed that mode A is less stable than mode B in flow past a cylindrical body. However, mode B can emerge before the other modes as the Reynolds number increases in the wake of a bluff-elongated cylinder (Ryan, Thompson & Hourigan 2005). Mode C emerges first as the Reynolds number increases in flow past a square cylinder with an incidence angle within a certain range (Yoon, Yang & Choi 2010), and in flow past an inclined flat plate (Yang *et al.* 2013). Thompson *et al.* (2006) found that mode QP becomes unstable before the other modes as the Reynolds number increases in flow past a normal flat plate.

In flow past a circular cylinder, Legendre, Lauga & Magnaudet (2009) predicted a delayed onset of shedding with increasing slip length and an extended steady separated wake with an arbitrary uniformly applied partial-slip boundary using direct numerical simulations. They also predicted that the vortex shedding frequency would be increased and the vortex intensity would be decreased at smaller slip lengths. Min & Kim (2005) showed that, in wall-bounded shear flows, the critical Reynolds number increases as streamwise slip increases. They found that although the transition to turbulence is delayed as streamwise slip increases, spanwise slip induces an earlier transition. Introducing a slip boundary could be expected to decrease the flow shear rate, so the critical Reynolds number could be expected to increase from steady to unsteady flow. However, the transition from unsteady two-dimensional flow to three-dimensional flow in the wake flow, which is homogeneous in the spanwise direction, or the transition to turbulent in a boundary layer flow, have different flow regimes by introducing slip surface.

In the transition from two- to three-dimensional flow, the flow shear rate of the base flow is supposed to be reduced with slip boundary. This decreases the probability of

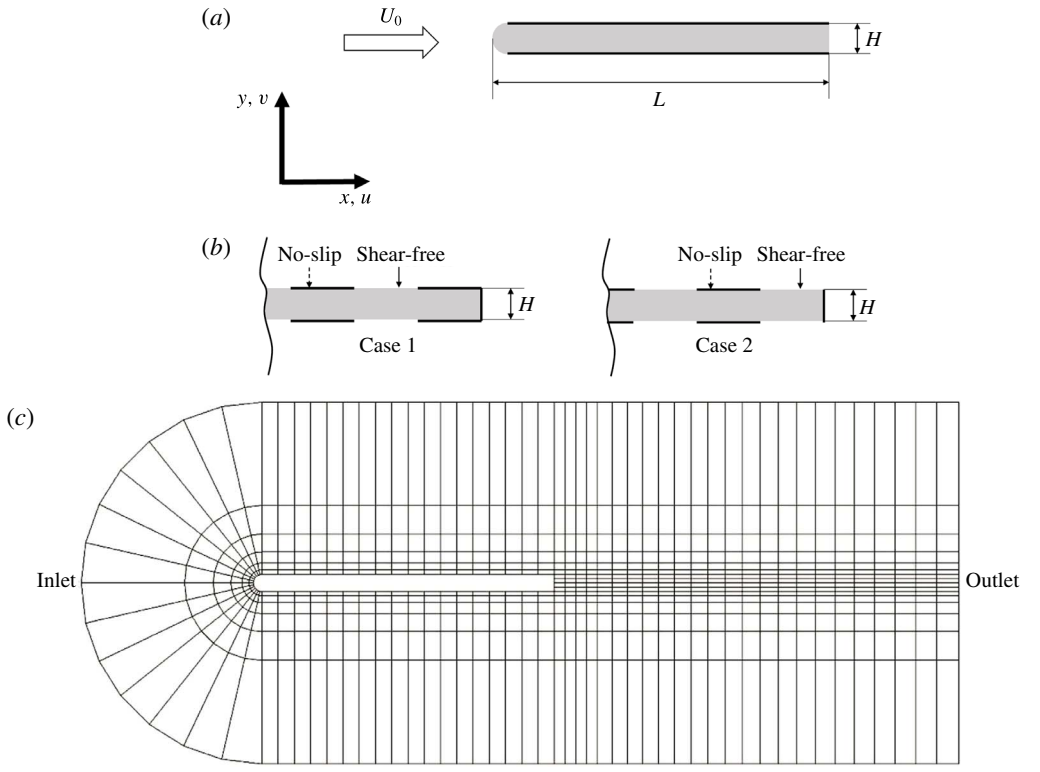

FIGURE 2. Schematic illustration of flow past an elongated bluff body. (*a*) The microgrates on the superhydrophobic surface were modelled using the upper and lower walls of a body consisting of repeating no-slip and slip boundary conditions. (*b*) Two superhydrophobic surface set-ups at the trailing edge. (*c*) One of the macroelement meshes used in the simulation.

evoking spanwise disturbances. However, damping of the spanwise disturbances also decreases when there is spanwise slip because the effect of viscous dissipation on spanwise fluctuations decreases as the slip velocity in the spanwise direction increases. In other words, the critical Reynolds number for three-dimensional instability depends on competition between base flow stability and the damping of disturbances in a spanwise direction. Here, we examine the effect of partial slip on three-dimensional instability in the wake of an elongated bluff body. We also examine the effects for a circular cylinder for comparative purposes.

2. Numerical method and validation

The flow considered is shown in figure 2. The cylindrical body consisted of a half-circle and a flat plate. The aspect ratio of the bluff body was defined as $AR = L/H$, where H and L are the thickness and length of the body, respectively. AR values of 2.4, 6.2, 11.8, 17.5, 23.2 and 28.8 were used to investigate the effect of aspect ratio. To avoid vortex shedding from the leading edge of the plate, the Reynolds number, defined as $Re = U_0 H/\nu$, where U_0 is the free-stream velocity and ν is the kinematic viscosity, was no larger than 900 (Welsh *et al.* 1990). The results showed that no vortex shedding occurred from the leading edge at Reynolds numbers within the range

investigated. As Re is large enough, minor boundary layer fluctuation can be observed along the plate. The upper and lower walls on the bluff body were covered by SHSs, which consisted of an array of micrograte aligned normal (transverse) to the flow direction, as shown in figure 2(*a*). The SHSs were modelled using boundary conditions at the wall with alternating regions of no-slip and shear-free boundary conditions (i.e. with spanwise slip), as shown in figure 1. This SHS model was first described by Martell, Perot & Rothstein (2009) and then by Park, Park & Kim (2013), Seo, Garcia-Mayoral & Mani (2015) and others. Different SHS designs were obtained mostly by varying two parameters: the pitch (P) and the gas fraction (GF), as well as by different trailing edge SHS arrangements. Here, GF is defined as $(P-W)/P$, where W is the width of the microgrates. We will consider two sets of parametric studies with the chosen aspect ratio: one set with a fixed GF of 0.5 and P/H values of 0.944, 1.214, 1.889, 3.4, 8.5 and 17, and the other with a fixed P/H of 1.889 and GF values of 0.5, 0.75 and 0.875. Two different set-ups (cases 1 and 2), based on the no-slip and shear-free boundary conditions at the trailing edge shown in figure 2(*b*), were considered.

A direct numerical simulation of flow past an elongated bluff body was performed using a spectral-element computational fluid dynamic package for time-dependent Navier–Stokes equations in a two-dimensional domain, with the two-dimensional flows serving as the basis for linear stability analysis. The governing equations can be written in non-dimensional form as:

$$\frac{\partial \boldsymbol{u}}{\partial t} + (\boldsymbol{u}\cdot\nabla)\boldsymbol{u} = -\nabla p + \frac{1}{Re}\nabla^2\boldsymbol{u}, \tag{2.1a}$$

$$\nabla\cdot\boldsymbol{u} = 0. \tag{2.1b}$$

The base flow could be obtained by solving (2.1*a*) and (2.1*b*) in two dimensions using a high-order spectral-element method. The governing equations were integrated forward in time using an operator splitting method to give third-order temporal accuracy. The code has been validated and successfully applied to several problems (Sheard 2011; Yang *et al.* 2013). The computational package has been described in detail by Sheard *et al.* (2007) and Sheard & Ryan (2007).

Floquet stability analysis was used to investigate the onset of secondary instability leading to three-dimensional flow. Using the Floquet theory, stability analysis was performed by decomposing the velocity and pressure field ($\boldsymbol{u}$, p) into a two-dimensional base flow ($\boldsymbol{U}$, P) and a three-dimensional disturbance ($\boldsymbol{u}'$, p'), as follows:

$$\boldsymbol{u} = \boldsymbol{U} + \boldsymbol{u}', \tag{2.2}$$

$$p = P + p'. \tag{2.3}$$

Substituting (2.2) and (2.3) into (2.1), cancelling out the base flow terms and disregarding the products of the perturbation field gave the linearized Navier–Stokes equations:

$$\frac{\partial \boldsymbol{u}'}{\partial t} + (\boldsymbol{U}\cdot\nabla)\boldsymbol{u}' + (\boldsymbol{u}'\cdot\nabla)\boldsymbol{U} = -\nabla p' + \frac{1}{Re}\nabla^2\boldsymbol{u}', \tag{2.4a}$$

$$\nabla\cdot\boldsymbol{u}' = 0. \tag{2.4b}$$

The disturbance field was further simplified by decomposing ($\boldsymbol{u}'$, p') into a Fourier series expansion in the spanwise direction, based on wavelength λ. The stability

N	Δt	St	C_D	C'_D	C'_L
6	0.004	0.2010	1.0528	0.0465	1.5459
8	0.002	0.2006	0.9906	0.0285	1.3749
10	0.001	0.2013	0.9853	0.0287	1.3720
12	0.001	0.2017	0.9939	0.0292	1.3732
14	0.0008	0.2017	0.9941	0.0292	1.3749

TABLE 1. Convergence of global quantities with different order N for case 1 ($AR = 17.5$, $P/H = 1.889$ and GF $= 0.5$, at $Re = 900$). The global quantities are the Strouhal number St ($St = fH/U_0$, based on the thickness of the body), the means and root mean squares of the fluctuating drag coefficients C_D and C'_D and the root mean square of the fluctuating lift coefficient C'_L.

behaviour was then reduced to a two-parameter problem using the Reynolds number and $\beta = 2\pi/\lambda$. The perturbation fields with different wavelengths were coupled with the T-periodic base flow, and this could be computed independently. Linear stability analysis was then performed by integrating the perturbation field forward in time, and the growth or decay of the field was monitored. Simplistically, the linear stability analysis is simplified as determining the eigenvalue of an ordinary differential equation with T-periodic solutions.

The eigenvalues corresponded to Floquet multipliers (μ), and the eigenvectors gave the modal shape of the perturbation field. A Floquet multiplier $|\mu| > 1$ indicated a positive growth rate and an unstable mode, and a Floquet multiplier $|\mu| < 1$ indicated a negative growth rate and a stable mode. The instability modes were classified as regular modes (modes A and B) with Floquet multipliers containing only positive real parts, a subharmonic mode (mode C) with only a negative real part and mode QP, with a complex conjugate pair of multipliers with a non-zero imaginary part.

The computational domain extended to $10H$ upstream, $25H$ downstream and $10H$ each side of the body. The domain was divided into macroelements, each of which contained $N \times N$ interpolation nodes. Free-stream boundary conditions were enforced at the upstream and lateral boundaries, and Neumann-type boundary conditions were used at the outlet. The most efficient mesh resolution for the simulation was determined by performing a grid resolution study for case 1 with $AR = 17.5$, $P/H = 1.889$, and GF $= 0.5$ at $Re = 900$. The results are shown in table 1. When the order $N \geqslant 12$, varying the number of mesh nodes barely affected the global quantities, so $N = 12$ was used in the simulations. One of the macroelement meshes used in the simulations is shown in figure 2(*c*). In this case, with $P/H = 1.889$, $N = 12$ gave a node number in one P of 23.

Blockage effects were assessed by performing a domain study for case 1 using $AR = 17.5$, $P/H = 1.889$, and GF $= 0.5$. As expected, the results showed that the Strouhal number was sensitive to the sidewall boundary width. A study was undertaken using case 1 ($AR = 17.5$, $P/H = 1.889$ and GF $= 0.5$) with a mesh $22H$ upstream, $40H$ downstream and $22H$ for each side of the body and 886 elements. The Floquet multipliers over the full range of β were calculated for this large domain. The critical Reynolds number for the transition from two- to three-dimensional flow was slightly affected by domain size, with a variation of approximately 3. The smaller domains mentioned above were used to study three-dimensional instability.

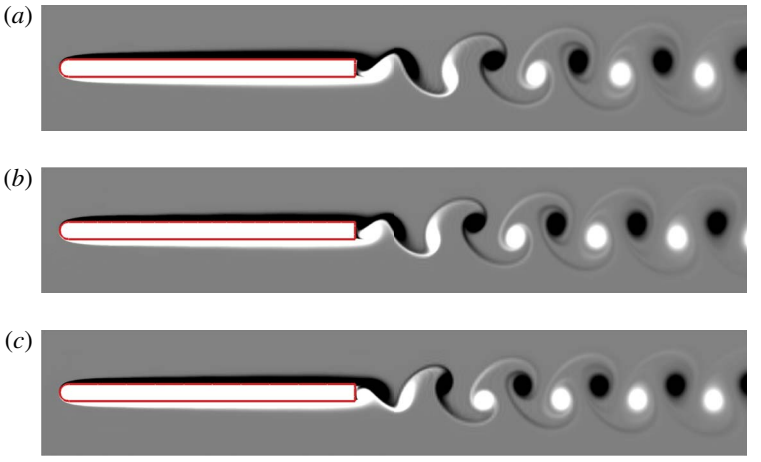

FIGURE 3. (Colour online) Instantaneous vorticity snapshots of (*a*) base flow for a regular body, (*b*) case 1 and (*c*) case 2 at $Re = 700$ and $AR = 17.5$. In both cases 1 and 2, $P/H = 3.4$ and $\mathrm{GF} = 0.5$.

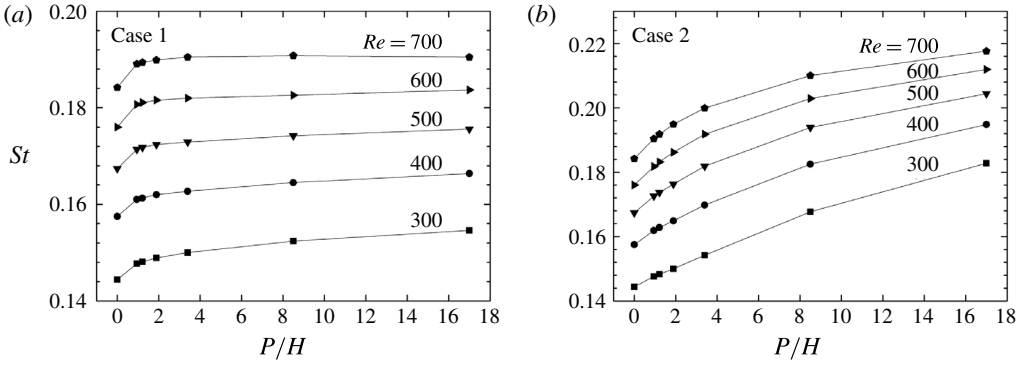

FIGURE 4. Strouhal number St as a function of pitch P/H, showing that the vortex shedding frequency is higher for a superhydrophobic than for a regular body ($AR = 17.5$).

3. Results and discussion

3.1. *Effects of SHSs on vortex shedding*

The two-dimensional base flow field results are summarized in this section to allow their comparison with the results of previous studies. The vorticity contours for the regular body case and cases 1 and 2 at $Re = 700$ and $AR = 17.5$ are shown in figure 3. The P and GF values were 3.4 and 0.5, respectively, for cases 1 and 2. The instantaneous vorticity snapshots of the base flow showed that the vortex shedding frequency increased with spanwise slip in both cases 1 and 2 because the numbers of vortices in the wakes increased.

Variations in the Strouhal number as a function of the P at a fixed GF of 0.5 and $AR = 17.5$ with varying Reynolds number are shown in figure 4. The results for a regular no-slip body ($P/H = 0$) are also shown; these indicate that the Strouhal number increased when a partial slip on the body was introduced in both cases 1 and 2, and that the Strouhal number increased further as the P increased. The main

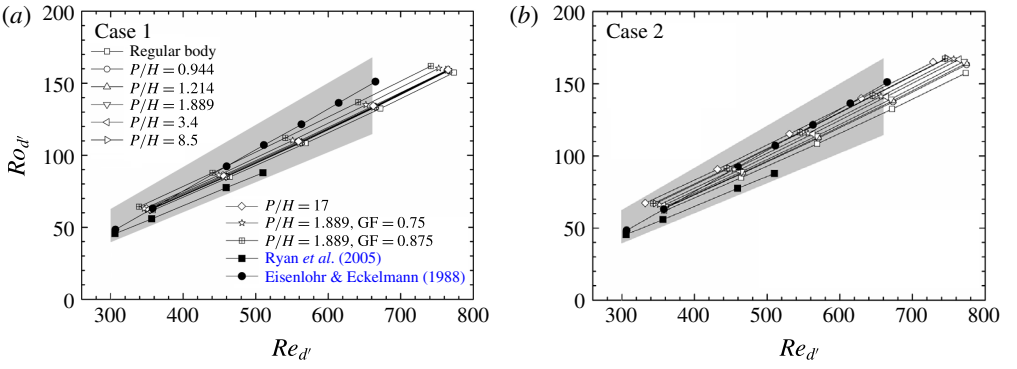

FIGURE 5. (Colour online) Roshko number Ro as a function of the Reynolds number Re based on d' ($AR = 17.5$). The shaded area indicates the spread of experimental data produced by Eisenlohr & Eckelmann (1988).

difference between cases 1 and 2 was caused by alternating the no-slip and shear-free boundary conditions of the elongated bluff body. Since the leading and trailing edges of the bluff body play the most important role for the outer flow, cases 1 and 2 are two extreme cases with totally different characteristics in those regions. Changing the slip characteristics between cases 1 and 2 therefore caused the flow to be modified over a wide range. Furthermore, at the same P length and with an SHS symmetrical in the y-direction, the aspect ratio of the plate is only a little higher than that in cases 1 and 2; i.e. there is an additional no-slip/slip part at the leading edge of case 1/2. Symmetrical SHSs were studied using $P/H = 3.4$ and GF $= 0.5$. The results showed that the symmetry of the SHS has little effect on the critical values for the different modes compared with the results for cases 1 and 2. This suggests that the slip properties at the trailing edges of the elongated bluff body are crucial for the effects of such SHSs.

The shedding frequencies, each in the form of a Roshko number Ro ($Ro = Re\,St$) as a function of the Reynolds number, are shown in figure 5. The spatial scaling parameter d' used in figure 5 was defined as $H + 2\delta$, with δ being the momentum thickness of the boundary layer measured at the trailing edge of the body. The results of a numerical simulation performed by Ryan *et al.* (2005) (in which flows past blunt trailing-edge bodies with different aspect ratios ($2.5 \leqslant AR \leqslant 17.5$) were simulated) and of experiments performed by Eisenlohr & Eckelmann (1988) (in which flows past blunt trailing-edge bodies with aspect ratios of $50 \leqslant AR \leqslant 800$ were conducted) are also shown in figure 5. A linear relationship between the Roshko and Reynolds numbers almost independent of the P was found for case 1. These results were comparable with the results of experiments performed by Eisenlohr & Eckelmann (1988) and of simulations performed by Ryan *et al.* (2005). The P influenced the Strouhal number less in case 1 than in case 2, even though the trends in Strouhal number were similar in both cases as the P increased. This suggests that vortex shedding in the wake may be strongly affected by slip characteristics at the trailing edge. It can be seen from figure 5(*b*) that the curves almost converge as the P decreases. This shows that the vortex shedding frequency is unaffected when there are sufficient P values. The Roshko–Reynolds number curves shifted upwards as the GF was increased in both cases.

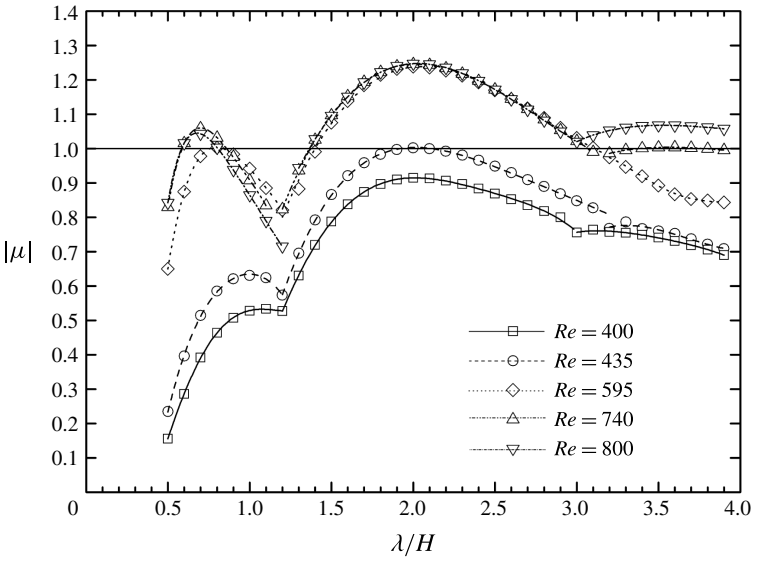

FIGURE 6. Floquet multipliers for the dominant modes plotted against the spanwise wavelengths for a regular bluff body at different Reynolds numbers and $AR = 17.5$.

3.2. *Floquet analysis with a no-slip boundary*

Floquet analysis was first performed for a regular bluff body with no-slip boundary conditions for a range of Reynolds numbers and $AR = 17.5$. Spanwise wavelengths in the range $0.5 < \lambda/H < 4.0$ were considered. The Floquet multipliers for a regular body are shown in figure 6. Three distinct stability branches can be observed. Similar results were found by Ryan (2004), Ryan *et al.* (2005) for flow past an elongated bluff body with a streamlined leading-edge geometry. A mode with similar spatio-temporal symmetry to that of mode B instability described by Williamson (1988) was found to become unstable first, at a critical Reynolds number $Re_c \approx 435$ when $\lambda/H = 2.0$. This mode is later called mode B′. The spatial structure of the streamwise vorticity of the perturbation field for the regular body case at $Re = 450$ and $\lambda/H = 2.0$ is shown in figure 7. This was similar to mode B for a circular cylinder, in which the streamwise vorticity sign was maintained from one half-cycle to the next. It can be seen in figure 6 that the Floquet multipliers did not increase further for the spanwise wavelength range of mode B′ when the Reynolds number increased above approximately 595.

At $\lambda/H \approx 0.8$, an instability mode with complex Floquet multipliers was observed, and the mode became critically unstable at $Re_c \approx 595$. Ryan (2004), Ryan *et al.* (2005) termed this mode S′. As the Reynolds number increased further, a mode corresponding to the longest wavelength became critically unstable at $Re_c \approx 740$ and $\lambda/H \approx 3.6$. This mode was topologically analogous to mode A for a circular cylinder wake; the unstable wavelength was also similar to mode A.

The neutral stability curves for the regular bluff body are shown in figure 8. It can be seen that the curve for mode S′ was closed (like an island) similar to mode C for flow past an inclined flat plate at a 20° angle of attack (Yang *et al.* 2013) and similar to mode A for flow past a rectangular cylinder with an AR of 0.125 (Choi & Yang 2014). Mode B′ for the regular body was less stable than modes S′ and A. In addition, unstable spanwise wavelengths for mode B′ occurred over a wide and

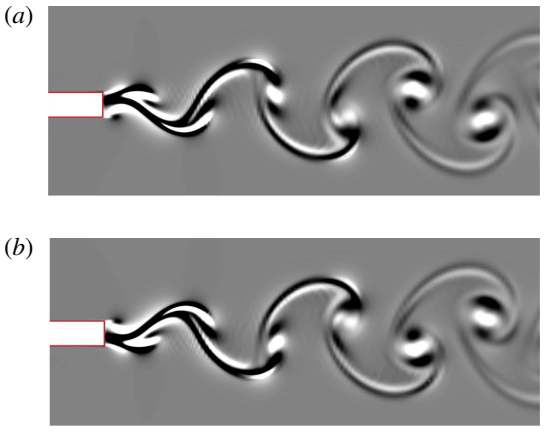

FIGURE 7. (Colour online) Streamwise vorticity field for the wake for the Floquet mode for a regular body ($AR = 17.5$, $Re = 450$, $\lambda/H = 2.0$). The images are separated by half the shedding cycle.

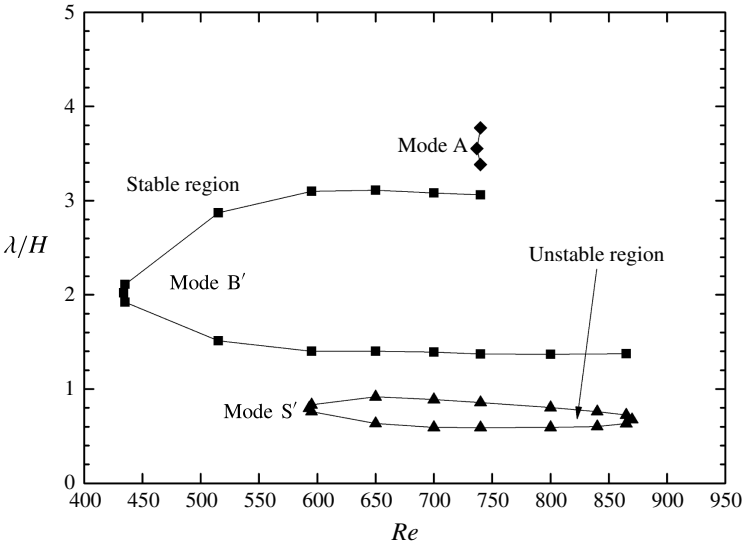

FIGURE 8. Neutral stability curves for a regular bluff body ($AR = 17.5$).

constant range after mode S′ had appeared, as shown in figure 6. It can also be seen from figure 6 that the Floquet multiplier was less than 1 at $\lambda/H \approx 3.2$ and $Re = 740$ and larger than 1 at $\lambda/H \approx 3.0$ and $Re = 800$. These wavelengths were the intersection points of the multipliers for modes B′ and A. This suggests that the neutral stability curves for modes B′ and A intersect at approximately $\lambda/H \approx 3.1$ when the Reynolds number increases above 740. The critical Reynolds numbers and wavelengths for the three different instability modes found by Ryan (2004) and in our study are shown in table 2. It can be seen that our results for modes B′ and A agree well with the results found by Ryan (2004). The Floquet multipliers for mode S′ determined by Ryan (2004) at $Re = 690$ were larger than 1, so the critical Reynolds number for mode S′ should be lower than 690.

	Present		Ryan (2004)	
	Re_c	λ/H	Re_c	λ/H
Mode B′	435	2.01	426	2.2
Mode S′	595	0.80	690	0.7
Mode A	740	3.55	718	3.5

TABLE 2. Critical Reynolds numbers and wavelengths for the three different instability modes for the wake behind an elongated bluff body ($AR = 17.5$) found in this study and that of Ryan (2004).

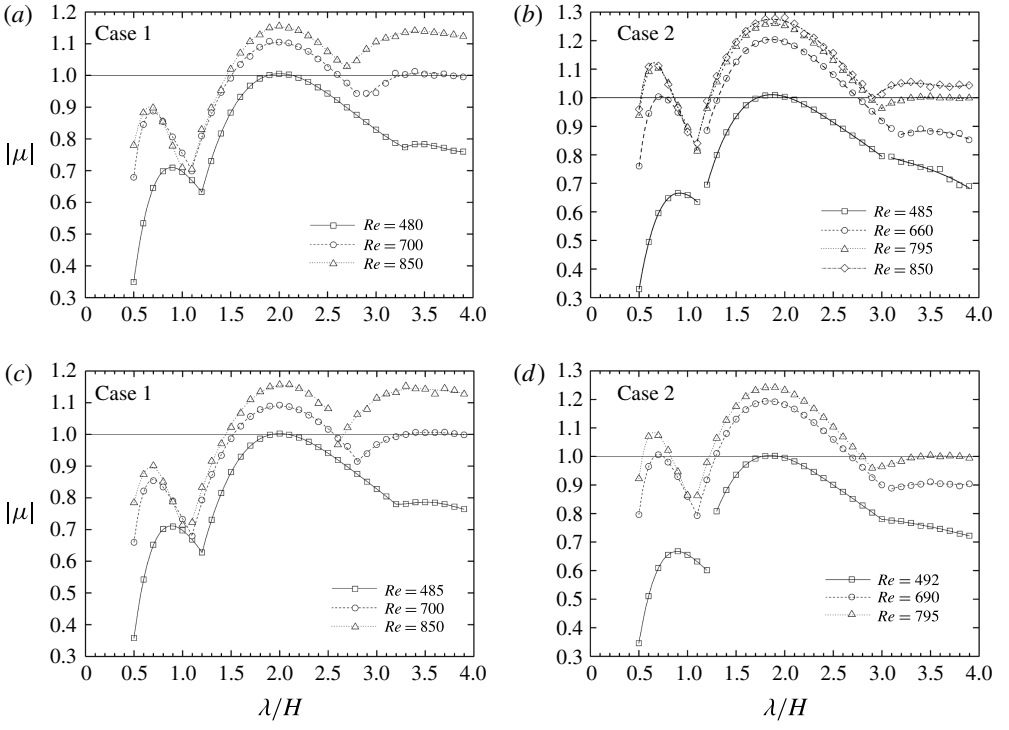

FIGURE 9. For caption see page 81.

3.3. *Effect of partial-slip conditions on three-dimensional instability at* GF = 0.5

The effect of the micrograte P on three-dimensional instability was first investigated by varying the micrograte P (i.e. the number of microgrates on the upper and lower surfaces of the body). The Floquet multipliers for $P/H = 0.944$, 1.214, 1.889, 3.4, 8.5 and 17, a fixed GF of 0.5, and a fixed AR of 17.5 are shown in figure 9 for case 1 (figure 9*a*,*c*,*e*,*g*,*i*,*k*) and case 2 (figure 9*b*,*d*,*f*,*h*,*j*,*l*). The corresponding neutral stability curves are shown in figure 10. The three stability branches that were observed for the regular body remained visible when the surfaces were covered with SHSs (figure 9). The most unstable mode in case 1 was mode B′. The critical Reynolds number for mode B′ increased from $Re_c \approx 435$ for the regular body to $Re_c \approx 500$ for case 1 because of the introduction of partial-slip conditions with $P/H = 0.944$. The critical Reynolds numbers for modes A and B′ changed slightly when P/H was changed from

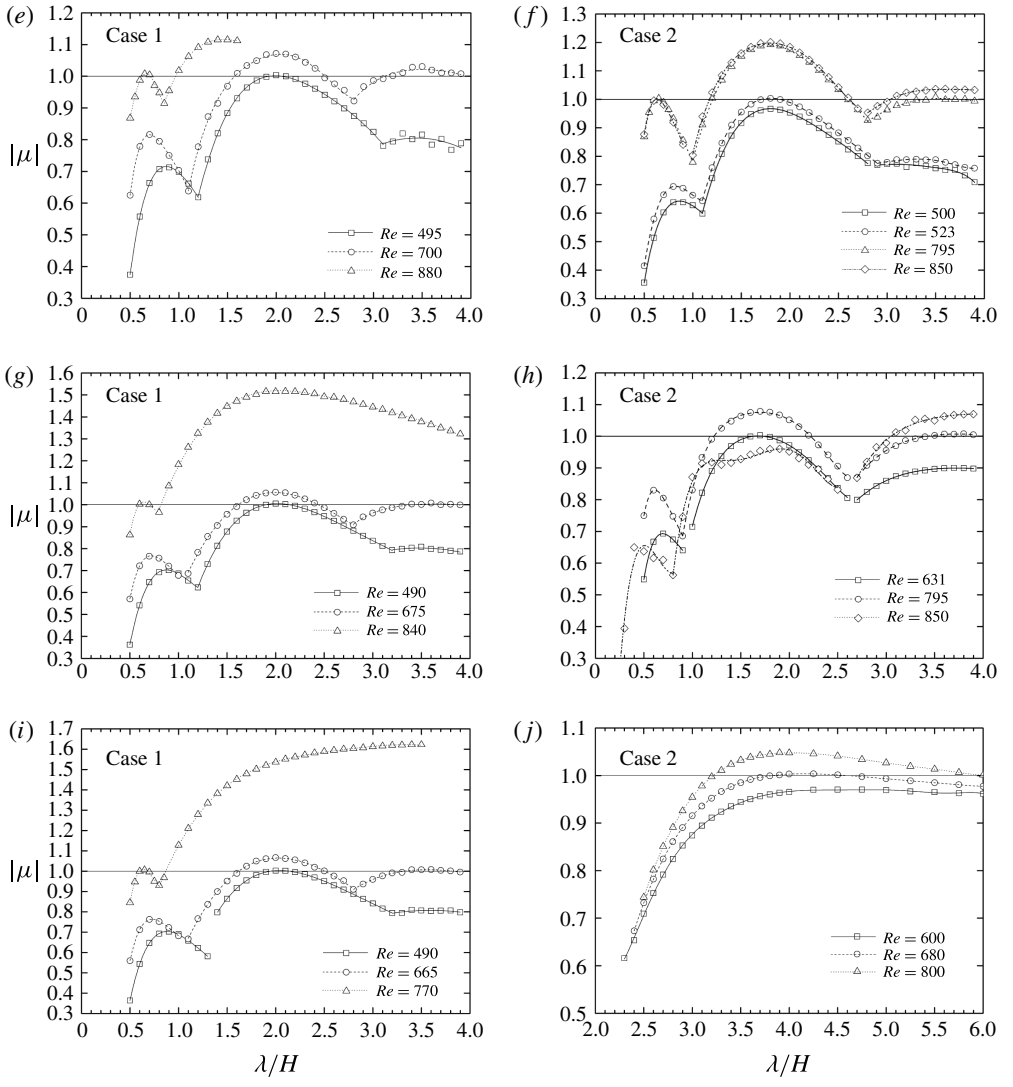

FIGURE 9 (cntd). For caption see next page.

0.944 to 17. Mode S′ was unstable at $P/H = 1.889$, 3.4 and 8.5, and the critical Reynolds numbers were larger for mode S′ than for modes A and B′.

In case 2, the influence of a partial slip on the body surfaces changed the critical Reynolds numbers dramatically, especially for modes B′ and S′. The neutral curves are shown in figure 10. These curves showed that mode B′ was still associated with a wide range of unstable spanwise wavelengths (compared with the results shown by modes S′ and A). However, the range of unstable wavelengths for mode B′ became narrower as the P increased because of large changes in the upper branch of each curve and slight changes in the lower branch. The unstable range for mode S′ decreased as the P increased. It can be seen from figure 9(*h*) that the flow was stable at spanwise wavelengths $\lambda/H < 0.9$ for Reynolds numbers up to 850, meaning that mode S′ disappeared at $P/H = 3.4$ (figure 10*h*).

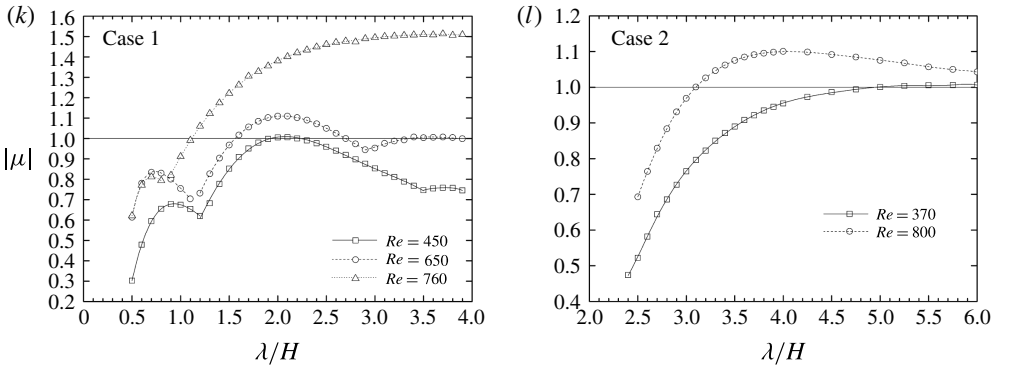

FIGURE 9 (cntd). Floquet multipliers for the dominant modes at a fixed GF of 0.5 for cases 1 and 2, with $AR = 17.5$, and (*a*,*b*) $P/H = 0.944$, (*c*,*d*) $P/H = 1.214$, (*e*,*f*) $P/H = 1.889$, (*g*,*h*) $P/H = 3.4$, (*i*,*j*) $P/H = 8.5$ and (*k*,*l*) $P/H = 17$.

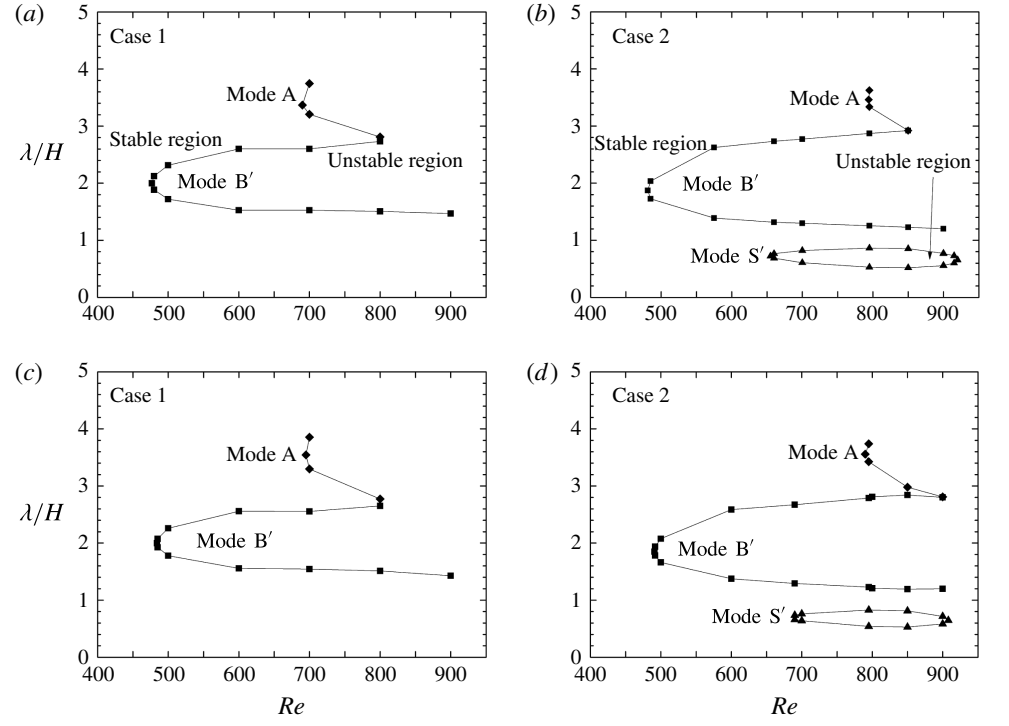

FIGURE 10. For caption see next page.

The neutral stability curves shown in figure 10 indicate that mode A was less affected than the other modes by changing the P, especially in case 1. However, the critical Reynolds number was higher when partial-slip conditions were introduced compared with the regular body (figure 8).

The relationships between the critical Reynolds numbers of the different three-dimensional instability modes and the P at a fixed GF of 0.5 are shown in figure 11(*a*,*b*), and the corresponding critical spanwise wavelengths (λ_c) are shown

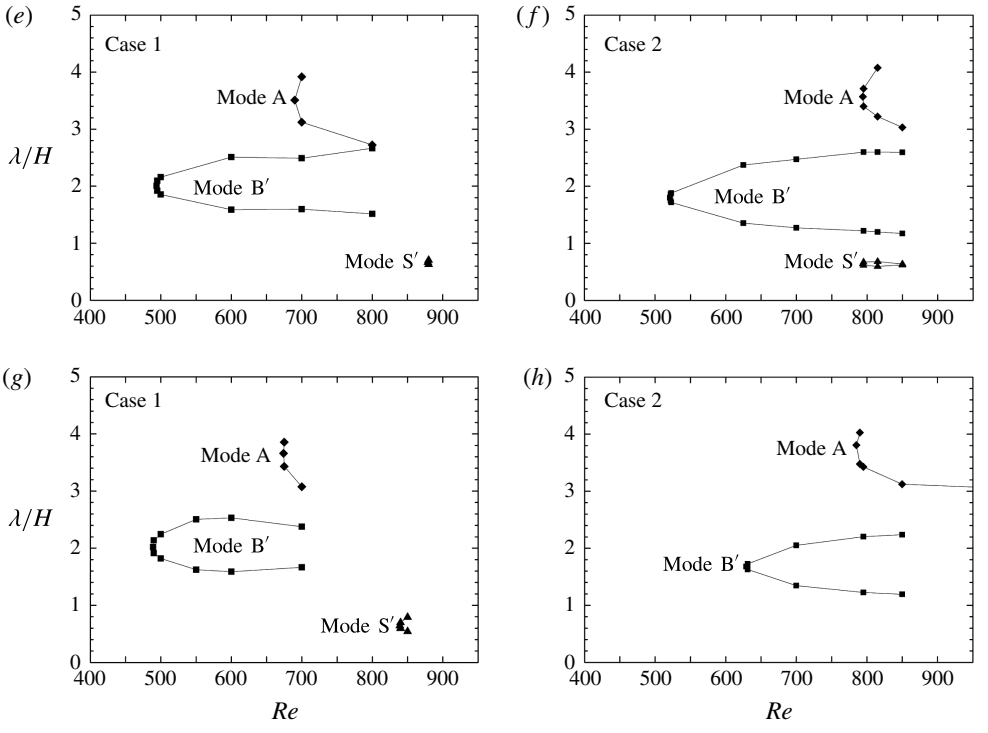

FIGURE 10 (cntd). Neutral stability curves for GF = 0.5 for cases 1 and 2, with $AR = 17.5$, and (*a*,*b*) $P/H = 0.944$, (*c*,*d*) $P/H = 1.214$, (*e*,*f*) $P/H = 1.889$ and (*g*,*h*) $P/H = 3.4$.

in figure 11(*c*,*d*). In case 1, mode S′ was more stable than modes A and B′, and the critical Reynolds number for mode S′ decreased as the P increased. However, the critical Reynolds numbers for modes A and B′ varied only slightly. In case 2, the critical Reynolds number for modes B′ and S′ increased with increases in P, and mode S′ disappeared altogether when P/H increased above 3.4. The critical Reynolds number for mode A was slightly higher for case 2 than for the regular body, and remained almost constant, while the P was less than the wavelength for mode A. The critical Reynolds number decreased dramatically as the P increased further. The dominant spanwise wavelengths for the different modes were almost unaffected by changes in the P, and were comparable to the corresponding modes for the regular body case (figure 11*c*,*d*).

Three-dimensional direct numerical simulations were conducted to validate the current study with SHSs. We selected case 1, with $AR = 17.5$, $P/H = 1.889$ and GF = 0.5. The simulations were performed using a consistent mesh in the x–y plane, assuming that the geometry would be homogeneous in the out-of-plane direction (z in Cartesian coordinates). This was achieved by expanding the flow variable in the out-of-plane direction using a Fourier expansion. The method was validated by Thompson, Leweke & Williamson (2001). In our simulation, a spanwise domain size of $12H$ was selected to allow all of the instability modes to fit inside the domain. Sixty-four Fourier planes were used for the computation. The instantaneous flow field for case 1 with $AR = 17.5$, $P/H = 1.889$ and GF = 0.5 at $Re = 600$ is shown in figure 12. The three-dimensional simulation was continued for more than 40 vortex shedding periods after the flow reached a quasi-steady state. The streamwise

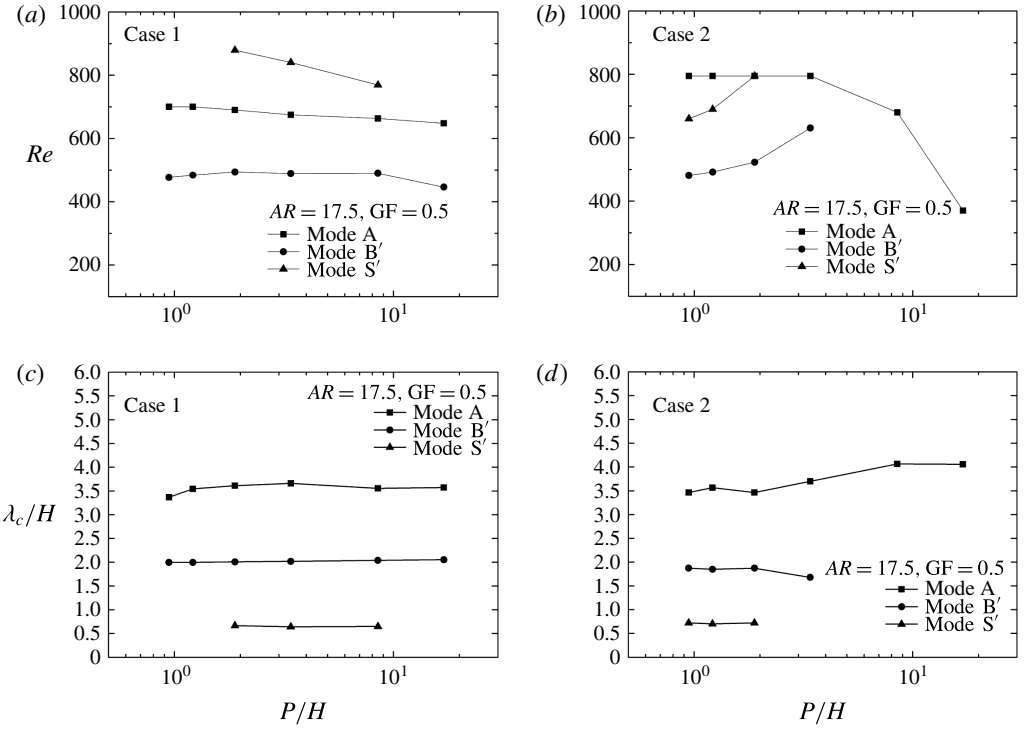

FIGURE 11. Relationships between the critical values for the three-dimensional instabilities and the pitch at a fixed GF of 0.5 and a fixed *AR* of 17.5. (*a*) and (*b*) The critical Reynolds numbers. (*c*) and (*d*) The dominant spanwise wavelengths.

and spanwise vorticity isosurfaces shown in figure 12 resembled mode B′ vortex structures. The spatial symmetry of the mode was identical to that of mode B′, and the wavelength was consistent with the critical wavelength of the Floquet mode found previously.

One may therefore conclude that the critical Reynolds number for three-dimensionality should be decreased by the presence of SHSs consisting of micrograte oriented transverse to the flow direction. Three-dimensional instability is generated through the growth in spanwise disturbances. With spanwise slip, spanwise disturbances are expected to be less damped due to a lack of viscous dissipation in the spanwise direction. However, the Floquet results showed that the critical Reynolds number for three-dimensionality increased. This could be because even though the damping of spanwise fluctuation weakens, it does not disappear with GF = 0.5. On the other hand, the spanwise disturbance is still dominated by the base flow. The evolution of the three-dimensional disturbance is delayed by using SHS; therefore, the critical Reynolds number of the three-dimensional instability increases.

3.4. *Gas fraction effect*

The effects of SHSs on the three-dimensional instability modes were assessed further using P/H values of 1.889 and 3.4, an *AR* of 17.5, and GFs of 0.5, 0.75 and 0.875. The Floquet multipliers for these cases are shown in figure 13. As described earlier, three instability modes were found for $P/H = 1.889$ and GF = 0.5 (figures 9*e*,*f* and

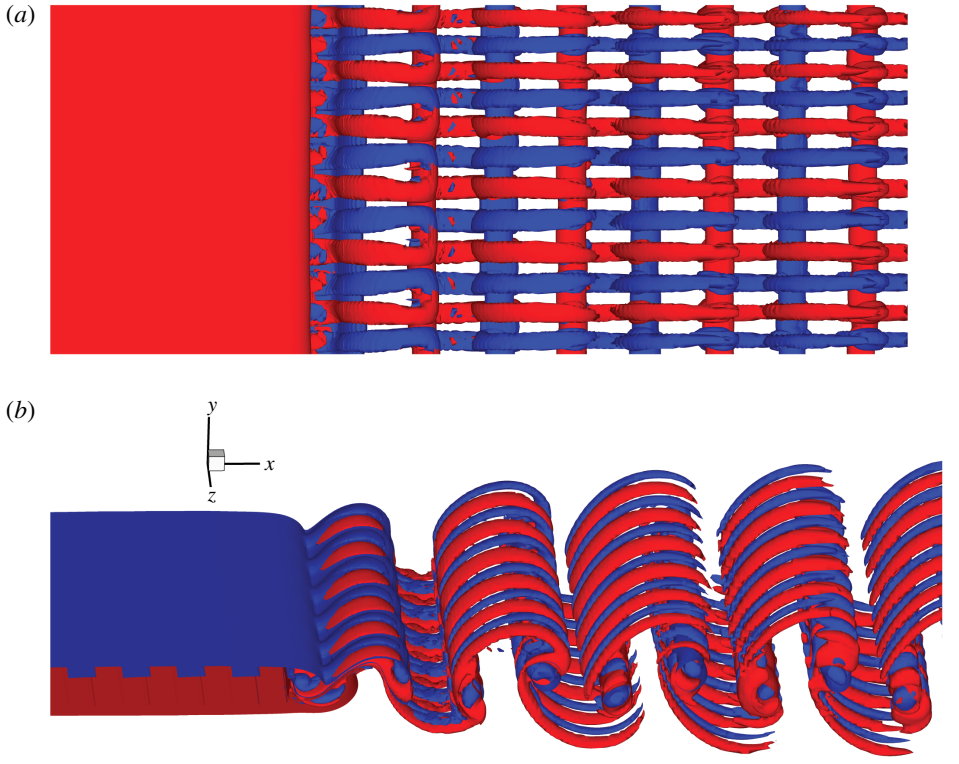

FIGURE 12. (Colour online) Three-dimensional view of the streamwise and spanwise vortices at $Re = 600$ (case 1, $AR = 17.5$, $P/H = 1.889$, and GF $= 0.5$). Blue, $\omega_x = 0.1$, $\omega_z = 1.0$; red, $\omega_x = -0.1$, $\omega_z = -1.0$.

10*e*,*f*). In case 1, the initial instability was mode A as the critical Reynolds number decreased when the GF increased to 0.75 and 0.875.

Three distinct stability branches were still visible in case 2, but only two, modes A and B′, appeared to be critically unstable. Unlike for $P/H = 1.889$ and GF $= 0.5$, mode A was less stable than mode B′ at GF $= 0.75$. The two modes merged into one and the instability tended to cover a fairly broad range of wavelengths as the Reynolds number increased further. At GF $= 0.875$ (figure 13*d*), no growing Floquet modes were found at $Re < 650$. Mode A became critically unstable at $Re \approx 650$ and $\lambda/H \approx 3.9$. A similar pattern was found at $P/H = 3.4$ and GF $= 0.75$ (figure 13*f*).

The critical Reynolds numbers in the different unstable modes at different GFs and at $P/H = 1.889$ are shown in table 3. Modes B′ and S′ both became more stable as the GF increased, indicating that either the critical Reynolds number increased or these modes disappeared. However, the critical Reynolds number for mode A decreased as the GF increased in both cases. As discussed earlier, the growth of three-dimensional disturbances depends on the base flow and the damping of disturbances caused by viscous dissipation. The base flow became more stable when SHSs were added, but the damping effect in the spanwise direction decreased at the same time, especially at high GFs. The kinetic energy of spanwise fluctuations was small when the disturbance wavelength was short, so viscous dissipation could have dampened the disturbances, even though the effect was weakened by spanwise slip. Modes B′ and S′ therefore became more stable as the GF increased, resulting in the base flow becoming more

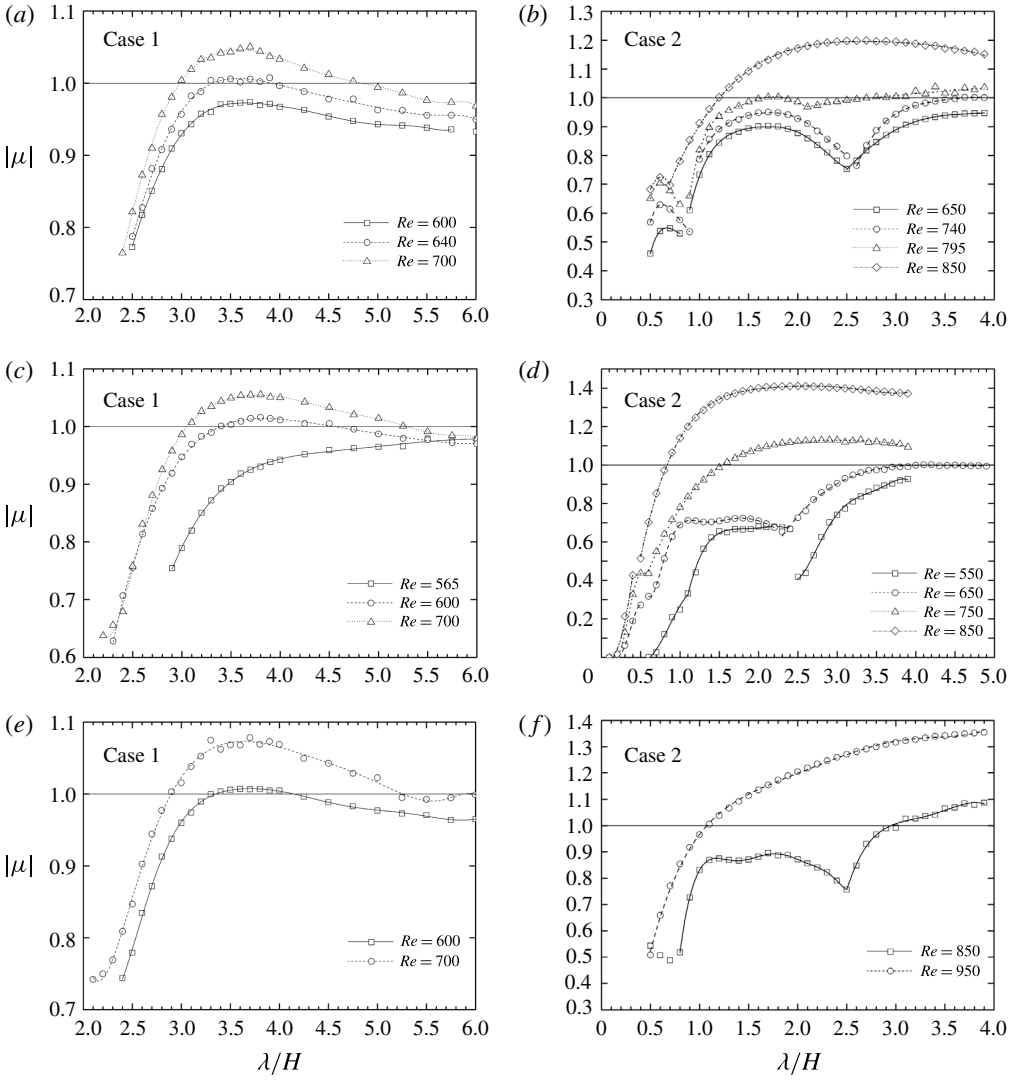

FIGURE 13. Floquet multipliers for the dominant modes at $AR = 17.5$ for (*a*,*c*,*e*) case 1 and (*b*,*d*,*f*) case 2. (*a*,*b*) $P/H = 1.889$ and $\mathrm{GF} = 0.75$. (*c*,*d*) $P/H = 1.889$ and $\mathrm{GF} = 0.875$. (*e*,*f*) $P/H = 3.4$ and $\mathrm{GF} = 0.75$.

stable. On the contrary, the disturbance with longer wavelengths, such as mode A, possesses more kinetic energy. As GF increases, the damping effect of spanwise disturbance weakens and becomes insufficient to dissipate the disturbance. In this way, the critical Reynolds number of mode A decreases as GF increases.

3.5. *Aspect ratio effect*

According to Ryan *et al.* (2005), the stability characteristics of an elongated bluff body with a streamlined leading-edge geometry are strongly affected by the aspect ratio. We used AR values of 2.4, 6.2, 11.8, 17.5, 23.2 and 28.8 with a fixed P/H of 1.889 and a fixed GF of 0.5 to determine whether the suggested variations caused by the slip surfaces changed qualitatively or quantitatively as the aspect ratio changed.

Case	GF	Mode B′	Mode S′	Mode A
Regular body	0	$Re_c \approx 435$	$Re_c \approx 595$	$Re_c \approx 740$
Case 1	0.5	$Re_c \approx 494$	$Re_c \approx 879$	$Re_c \approx 690$
	0.75	None	None	$Re_c \approx 640$
	0.875	None	None	$Re_c \approx 590$
Case 2	0.5	$Re_c \approx 523$	$Re_c \approx 795$	$Re_c \approx 795$
	0.75	$Re_c \approx 795$	None	$Re_c \approx 740$
	0.875	None	None	$Re_c \approx 650$

TABLE 3. Gas fraction effect on the critical Reynolds number at $P/H = 1.889$ and $AR = 17.5$ for cases 1 and 2.

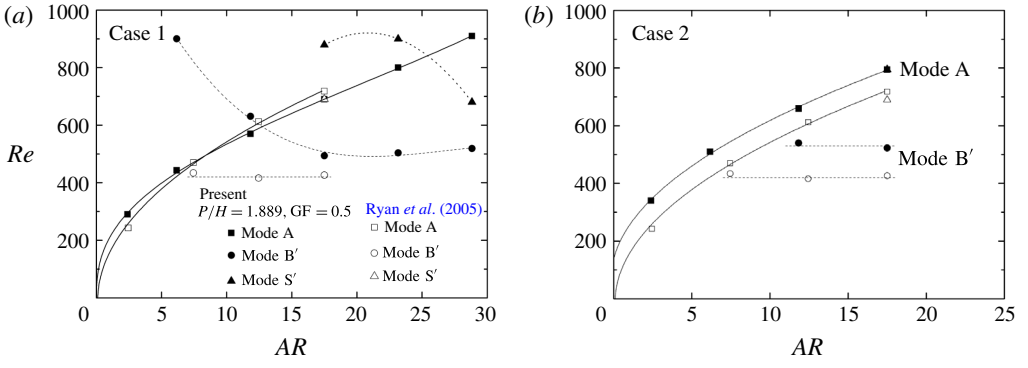

FIGURE 14. (Colour online) Critical Reynolds numbers for the different mode transitions plotted against the aspect ratios for (*a*) case 1 and (*b*) case 2. The curves are approximate fits to the data.

The AR values of 2.4, 6.2, 11.8, 17.5, 23.2 and 28.8 corresponded to micrograte numbers of 1, 3, 6, 9, 12 and 15, respectively. The critical Reynolds numbers for the different three-dimensional mode transitions are plotted against the cylinder aspect ratios in figure 14. The results found by Ryan *et al.* (2005) are also plotted for comparison.

In case 1, the critical Reynolds numbers of the different modes varied when different aspect ratios were used. The critical Reynolds number for mode A increased as the aspect ratio increased. However, the critical Reynolds numbers for modes B′ and S′ were different, so the mode sequence when different unstable modes occurred differed for different aspect ratios. In case 2, the critical Reynolds numbers for the different modes changed by a fixed amount because of the SHSs used for all aspect ratios. In general, three-dimensional stability improved when additional SHSs were added in both cases 1 and 2 for the different aspect ratios, as demonstrated by the increase in the critical Reynolds number.

The streamwise vorticity field for the Floquet mode for case 1, at $AR = 2.4$, $P/H = 1.889$, $\mathrm{GF} = 0.5$, $Re = 450$ and $\lambda/H = 2.0$, is shown in figure 15. The spatio-temporal symmetry and perturbation field distribution for this mode were analogous to those of mode A instability in flow past a circular cylinder. It can be seen from figure 15 that, at the same spanwise location, the streamwise vorticity swapped signs every half vortex shedding cycle.

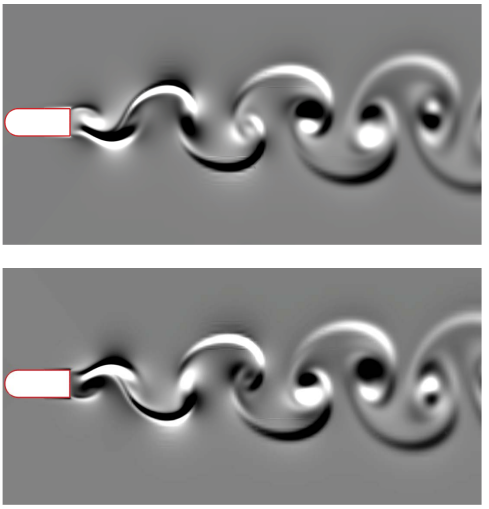

FIGURE 15. (Colour online) Wake streamwise vorticity field of the Floquet mode for mode A of case 1 ($AR = 2.4$, $P/H = 1.889$, GF $= 0.5$, $Re = 300$ and $\lambda/H = 4.0$). The images are separated by half the shedding cycle.

3.6. *Effect of the geometric configuration of the SHSs*

Besides the P and GF, the geometric configuration of the SHSs can also affect the slip characteristics and flow behaviour (Rastegari & Akhavan 2015). The results above show that the SHSs increased the critical Reynolds number of the three-dimensionality in both cases 1 and 2. However, the Reynolds numbers at which distinct modes became critical were different in cases 1 and 2, as shown in figure 10. In fact, there are an infinite number of geometric SHS configurations, and cases 1 and 2 are two extreme configurations. Because the leading and trailing edges are the most influential positions on an elongated bluff body, swapping slip and no-slip properties at these positions modifies the flow, as shown by the different Floquet multipliers found for cases 1 and 2 (figure 16*b*). Cases 1a and 2a (illustrated in figure 16*a*) were designed to emphasize the importance of the leading and trailing edges. Cases 1a and 2a had the same P lengths as the original cases, but the SHS arrangement was symmetrical in the y-direction in cases 1a and 2a. In other words, the new cases 1a and 2a had exactly the same slip characteristics at the trailing edges as cases 1 and 2, but opposite slip characteristics in the middle of the elongated bluff body. The Floquet multipliers were almost the same for cases 1a and 2a and cases 1 and 2, respectively, as shown in figure 16(*b*).

While the trailing edge was not cut at an integer multiple P, such as in case 1b, it was obtained by decreasing half the no-slip part at the trailing edge. To give case 1b the same aspect ratio as case 1, the no-slip part removed from the trailing edge was added to the leading edge in the SHS area. The same SHS arrangements were used for case 2b. It is evident that the Floquet multipliers for cases 1b and 2b are between the two extremes found for cases 1 and 2 (figure 16*b*), which suggests that as the modification of geometric configuration of SHSs, the critical Reynolds number of three-dimensional instability is different. The exact critical Reynolds number should be in the range between the critical values of cases 1 and 2. Regardless, the introduction of SHSs can eventually delay the three-dimensional instability.

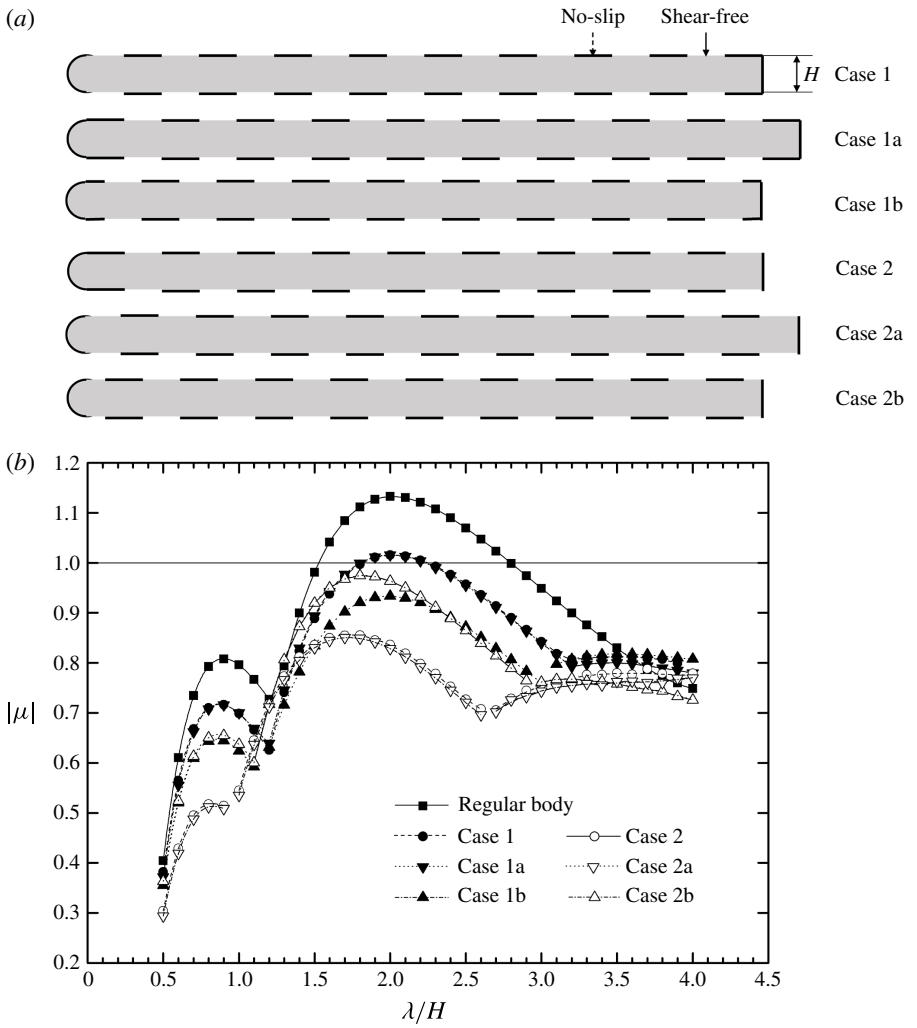

FIGURE 16. (*a*) Superhydrophobic surface set-ups with $P/H = 3.4$ and GF $= 0.5$. (*b*) Floquet multipliers for the dominant modes for the cases shown in (*a*) and the regular body case. The Reynolds number was 500 in each case.

3.7. *Mode characteristics*

In previous studies (Williamson 1996; Leweke & Williamson 1998; Thompson *et al.* 2001), it was suggested that mode A is predominantly an elliptical instability that can have a range of wavelengths varying from 3–4.5 cylinder diameters. The dispersion is caused by the flow phases in which mode A is less regular. The present study shows that both modes B′ and S′ are suppressed as the area of the body surface covered by shear-free conditions increases. Mode A will eventually become the initial instability mode. However, the results for mode A in cases 1 and 2 were found to be different. This reflects slip conditions at the trailing edge of the elongated bluff body, which severely affect mode A. We used a circular cylinder with alternative slip and no-slip boundary conditions to avoid this effect.

We investigated flow past a circular cylinder coated with SHSs to investigate the effects of partial-slip conditions on mode A instability. Two P values, $P/D = 0.349$

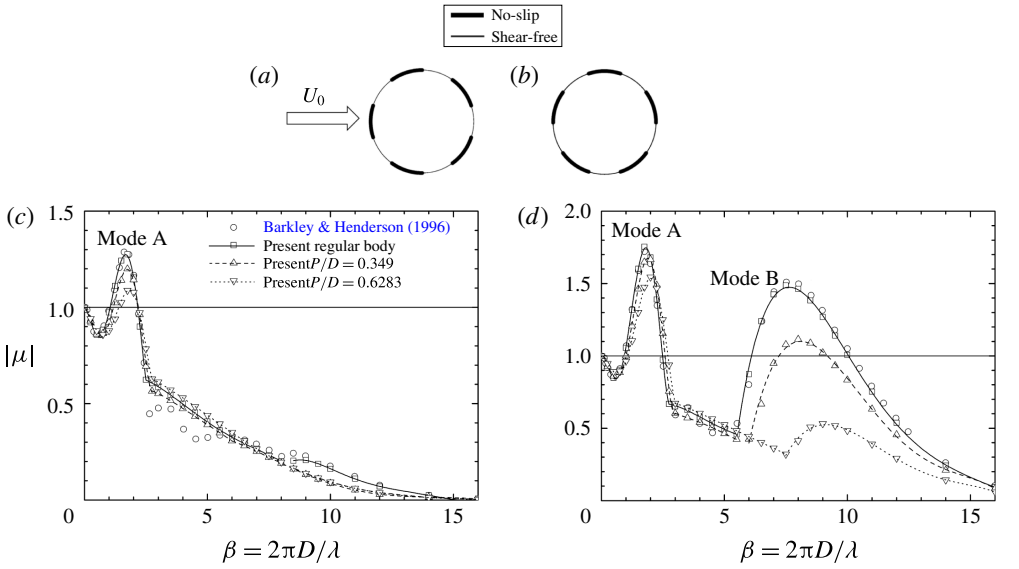

FIGURE 17. (Colour online) (*a*,*b*) Schematic illustrations of flow past a circular cylinder with different no-slip and shear-free boundary conditions. (*c*,*d*) Moduli of the Floquet multipliers plotted against the spanwise wavenumber β ($\beta = 2\pi D/l$, where D is the cylinder diameter) for flow past circular cylinders with different pitches at (*c*) $Re = 220$ and (*d*) $Re = 280$. The results of a previous study (Barkley & Henderson 1996) are also shown for comparison.

and 0.6283, and a fixed GF of 0.5, were used. We previously published the numerical method used and a validation of the Floquet stability analysis for flow past a circular cylinder (Yang *et al.* 2013).

The two different SHS arrangements simulated are shown in figure 17(*a*,*b*). The Strouhal numbers for these two arrangements were only 0.01 different at $Re = 220$. The arrangement shown in figure 17(*a*) was symmetrical in the flow direction and gave a lower Strouhal number than the arrangement shown in figure 17(*b*). Therefore, the set-up in figure 17(*a*) was adopted for the following simulations.

The Floquet multipliers for different spanwise wavenumbers β at $Re = 220$ and $Re = 280$ for flow past a circular cylinder are shown in figure 17. The effects of the SHSs are presented to allow comparison of the results for the regular body and the SHS-coated body. The Floquet multipliers for instability mode B decreased dramatically when partial-slip conditions on the cylinder surface were introduced by adding SHSs. The Floquet multipliers for instability mode A also slightly decreased when the SHSs were added. The neutral stability curves for modes A and B determined in a previous study (Posdziech & Grundmann 2001) are shown in figure 18. The most unstable spanwise wavelengths calculated from the maximum Floquet multipliers are also included. Our results agreed well with the results of the previous study for the regular body. The unstable spanwise wavelength ranges became narrower when SHSs were added for both modes A and B at $P/D = 0.349$. Mode B was suppressed at $Re = 280$ and $P/D = 0.6283$. The most unstable spanwise wavelengths decreased because of the partial-slip effect. However, the lower parts of the neutral stability curves remained almost unchanged.

The streamwise vorticity contours for modes A and B are plotted in figures 19 and 20 to indicate the mode symmetries. It can be seen that the mode symmetries

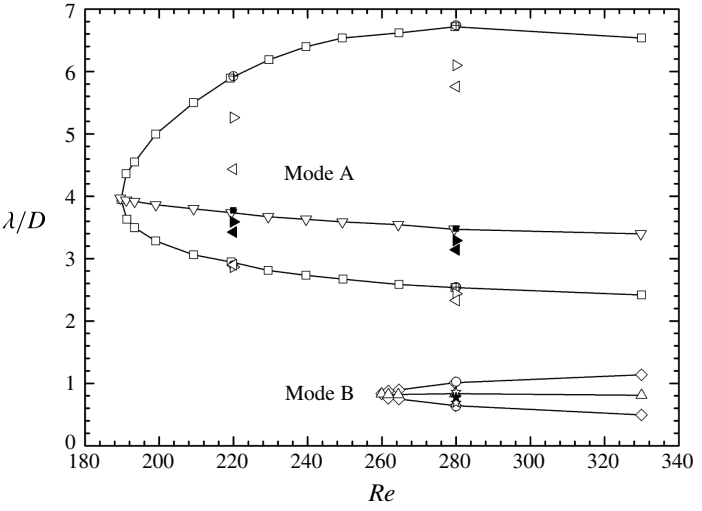

FIGURE 18. Neutral stability curves and the most unstable wavelengths for flow past a circular cylinder. —— Posdziech & Grundmann (2001) (□ neutral curve mode A, ◇ neutral curve mode B, ▽ the most unstable wavelength mode A, △ the most unstable wavelength mode B). The results of this work for the regular body (⊕ mode A, ■ the most unstable wavelength mode A, ○ mode B, ◆ the most unstable wavelength mode B), $P/D = 0.349$ (▷ mode A, ▶ the most unstable wavelength mode A, ☆ mode B, ★ the most unstable wavelength mode B), and $P/D = 0.6283$ (◁ mode A, ◀ the most unstable wavelength mode A) are also shown.

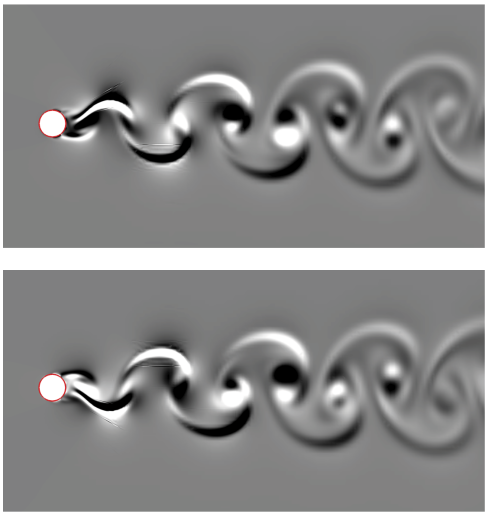

FIGURE 19. (Colour online) Wake streamwise vorticity field of the Floquet mode for mode A ($P/D = 0.6283$, GF $= 0.5$, $Re = 220$ and $\lambda/D = 3.59$). The images are separated by half the shedding cycle.

were not affected by adding SHSs. For the circular cylinder, the perturbation vorticity of mode B decayed downstream much more quickly than the perturbation vorticity of mode A. Similar downstream decay was found for the unstable mode B′ in the wake of the elongated bluff body, as described in the previous sections. This was because

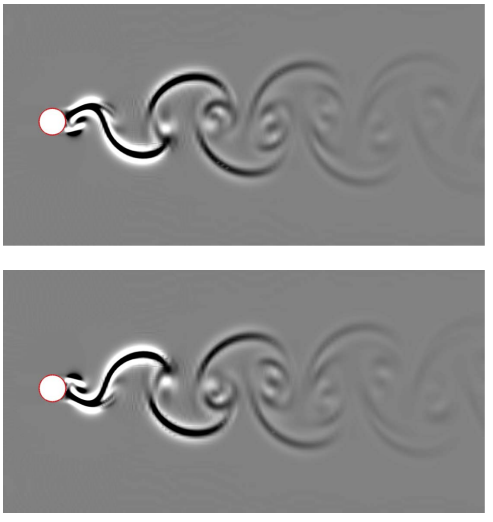

FIGURE 20. (Colour online) Wake streamwise vorticity field of the Floquet mode for mode B ($P/D = 0.349$, GF $= 0.5$, $Re = 280$ and $\lambda/D = 0.785$). The images are separated by half the shedding cycle.

mode B as considered here had a relatively short spanwise wavelength, and the flow structures had lower energies and would be subject to viscous diffusion. Since the wavelength of mode B is much shorter than that of mode A, the kinetic energy of spanwise fluctuation of mode B can be quickly dissipated by the viscosity of fluid. For the same reason, one can conclude that the shorter wavelengths of the unstable modes tend to be more easily suppressed by SHSs. This finding agrees with the results of all instability analyses performed in this study.

4. Summary and concluding remarks

We performed numerical simulations to study the influence of partial-slip boundary conditions on three-dimensional instability in the wake behind a bluff body. An elongated bluff body was considered, and a circular cylinder was used for comparative purposes. SHSs consisting of microgrates oriented normal to the flow direction were modelled under shear-free boundary conditions assuming that the air–water regions were flat. When compared with a regular body, the two-dimensional base flow showed some phenomena similar to that found by other researchers, such as an increased vortex shedding frequency and a linear relationship between the Roshko and Reynolds numbers, independent of partial-slip conditions.

Floquet stability analyses were performed to investigate the effects of the SHSs on three-dimensional instability in set-ups with two different SHS boundary conditions (cases 1 and 2). Cases 1 and 2 correspond to two extreme situations that limit the range of the influence of SHS. Three modes were found for a regular body. These were comparable to modes A, B′ and S′ for flow past a streamlined leading-edge body. These instability modes had some similarities and differences with modes A, B and QP, which have previously been identified in flow past circular and square cylinders.

The effects of the SHS geometries (i.e. the P and GF) were examined, and both the flow behaviour and the critical Reynolds number were found to be strongly affected when the no-slip and shear-free boundary conditions were swapped. Partial-slip

conditions appeared to delay the onset of three-dimensional instability, especially for modes B′ and S′ in cases 1 and 2. The critical Reynolds number for instability mode A was slightly affected by the SHSs when the P decreased. The critical spanwise wavelengths for the three modes were almost unaffected by the SHSs, and were comparable to the critical spanwise wavelengths for a regular body. The critical Reynolds numbers for different unstable modes changed markedly when the GF increased. Increasing the GF decreased the critical Reynolds number of mode A, but the critical Reynolds numbers for the unstable modes B′ and S′ either increased or disappeared altogether. Therefore, mode A could become initially unstable during the transition to three-dimensional flow in the wake of an elongated body by SHSs.

The elongated bluff-body aspect ratio strongly affected the three-dimensional instability modes with or without the presence of SHSs. The critical Reynolds number for three-dimensional instability increased when SHSs were present at any given aspect ratio.

The results for flow past a circular cylinder coated with SHSs had similar characteristics to the results found for an elongated body, including the critical Reynolds numbers for modes A and B being delayed and the unstable spanwise wavelength range becoming narrower.

Acknowledgements

This work was supported by the National Natural Science Foundation of China (nos 11502086 and 11502087) and Fundamental Research Funds for the Central Universities (nos 2015QN141, 2015QN018, 2015MS105).

REFERENCES

BARKLEY, D. & HENDERSON, R. D. 1996 Three-dimensional Floquet stability analysis of the wake of a circular cylinder. *J. Fluid Mech.* **322**, 215–241.

BLACKBURN, H. M. & SHEARD, G. J. 2010 On quasiperiodic and subharmonic Floquet wake instabilities. *Phys. Fluids* **22**, 031701.

CARMO, B. S., SHERWIN, S. J., BEARMAN, P. W. & WILLDEN, R. H. J. 2008 Wake transition in the flow around two circular cylinders in staggered arrangements. *J. Fluid Mech.* **597**, 1–29.

CHOI, C. B. & YANG, K. S. 2014 Three-dimensional instability in flow past a rectangular cylinder ranging from a normal flat plate to a square cylinder. *Phys. Fluids* **26**, 061702.

DANIELLO, R., MURALIDHAR, P., CARRON, N., GREENE, M. & ROTHSTEIN, J. P. 2013 Influence of slip on vortex-induced motion of a superhydrophobic cylinder. *J. Fluid Struct.* **42**, 358–368.

DELAUNAY, Y. & KAIKTSIS, L. 2001 Control of circular cylinder wakes using base mass transpiration. *Phys. Fluids* **13**, 3285–3302.

DONG, S., TRIANTAFYLLOU, G. S. & KARNIADAKIS, G. E. 2008 Elimination of vortex streets in bluff-body flows. *Phys. Rev. Lett.* **100** (20), 204501.

EISENLOHR, H. & ECKELMANN, H. 1988 Observation in the laminar wake of a thin flat plate with a blunt trailing edge. In *Proceedings of the Conference on Experimental Heat Transfer, Fluid Mechanics, and Thermodynamics*, pp. 264–268. Elsevier.

FLYNN, M. R. & BUSH, J. W. M. 2008 Underwater breathing: the mechanics of plastron respiration. *J. Fluid Mech.* **608**, 275–296.

LECORDIER, J. C., HAMMA, L. & PARANTHOEN, P. 1991 The control of vortex shedding behind heated circular cylinders at low Reynolds numbers. *Exp. Fluids* **10**, 224–229.

LEGENDRE, D., LAUGA, E. & MAGNAUDET, J. 2009 Influence of slip on the dynamics of two-dimensional wakes. *J. Fluid Mech.* **633**, 437–447.

LEWEKE, T. & WILLIAMSON, C. H. K. 1998 Three-dimensional instabilities in wake transition. *Eur. J. Mech. (*B/Fluid*)* **17**, 571–586.

MARQUES, F., LOPEZ, J. M. & BLACKBURN, H. M. 2004 Bifurcations in systems with $Z(2)$ spatio-temporal and $O(2)$ spatial symmetry. *Phys.* D **189**, 247–276.

MARTELL, M. B., PEROT, J. B. & ROTHSTEIN, J. P. 2009 Direct numerical simulations of turbulent flows over superhydrophobic surfaces. *J. Fluid Mech.* **620**, 31–41.

MASTROKALOS, M. E., PAPADOPOULOS, C. I. & KAIKTSIS, L. 2015 Optimal stabilization of a flow past a partially hydrophobic circular cylinder. *Comput. Fluids* **107**, 256–271.

MENEGHINI, J. R., CARMO, B. S., TSILOUFAS, S. P., GIORIA, R. S. & ARANHA, J. A. P. 2011 Wake instability issues: from circular cylinders to stalled airfoils. *J. Fluid Struct.* **27**, 694–701.

MIN, T. & KIM, J. 2005 Effects of hydrophobic surface on stability and transition. *Phys. Fluids* **17**, 108106.

MITTAL, S. & RAGHUVANSHI, A. 2001 Control of vortex shedding behind circular cylinder for flows at low Reynolds numbers. *Intl J. Numer. Meth. Fluids* **35**, 421–447.

MURALIDHAR, P., FERRER, N., DANIELLO, R. & ROTHSTEIN, J. P. 2011 Influence of slip on the flow past superhydrophobic circular cylinders. *J. Fluid Mech.* **680**, 459–476.

PARK, H., PARK, H. & KIM, J. 2013 A numerical study of the effects of superhydrophobic surface on skin-friction drag in turbulent channel flow. *Phys. Fluids* **25**, 110815.

PARK, H., SUN, G. Y. & KIM, C. J. 2014 Superhydrophobic turbulent drag reduction as a function of surface grating parameters. *J. Fluid Mech.* **747**, 722–734.

POSDZIECH, O. & GRUNDMANN, R. 2001 Numerical simulation of the flow around an infinitely long circular cylinder in the transition regime. *Theor. Comput. Fluid Dyn.* **15**, 121–141.

RASTEGARI, A. & AKHAVAN, R. 2015 On the mechanism of turbulent drag reduction with super-hydrophobic surfaces. *J. Fluid Mech.* **773**, R4.

ROACH, P., SHIRTCLIFFE, N. J. & NEWTON, M. I. 2008 Progess in superhydrophobic surface development. *Soft Matt.* **4**, 224–240.

ROBICHAUX, J., BALACHANDAR, S. & VANKA, S. P. 1999 Three-dimensional Floquet instability of the wake of square cylinder. *Phys. Fluids* **11**, 560–578.

ROSHKO, A. 1955 On the wake and drag of bluff bodies. *J. Aero. Sci.* **22**, 124–132.

ROTHSTEIN, J. P. 2010 Slip on Superhydrophobic Surfaces. *Annu. Rev. Fluid Mech.* **42**, 89–109.

RYAN, K. 2004 The analysis of wake structures behind stationary, freely oscillating and tethered cylinders. PhD thesis, Department of Mechanical Engineering, Monash University, Victoria, Australia.

RYAN, K., THOMPSON, M. C. & HOURIGAN, K. 2005 Three-dimensional transition in the wake of bluff elongated cylinders. *J. Fluid Mech.* **538**, 1–29.

SEO, J., GARCIA-MAYORAL, R. & MANI, A. 2015 Pressure fluctuations and interfacial robustness in turbulent flows over superhydrophobic surfaces. *J. Fluid Mech.* **783**, 448–473.

SHEARD, G. J. 2011 Wake stability features behind a square cylinder: focus on small incidence angles. *J. Fluid Struct.* **27**, 734–742.

SHEARD, G. J., FITZGERALD, M. J. & RYAN, K. 2009 Cylinders with square cross-section: wake instabilities with incidence angle variation. *J. Fluid Mech.* **630**, 43–69.

SHEARD, G. J., LEWEKE, T., THOMPSON, M. C. & HOURIGAN, K. 2007 Flow around an impulsively arrested circular cylinder. *Phys. Fluids* **19**, 083601.

SHEARD, G. J. & RYAN, K. 2007 Pressure-driven flow past spheres moving in a circular tube. *J. Fluid Mech.* **592**, 233–262.

SHEARD, G. J., THOMPSON, M. C. & HOURIGAN, K. 2003 From spheres to circular cylinders: the stability and flow structures of bluff ring wakes. *J. Fluid Mech.* **492**, 147–180.

THOMPSON, M. C., HOURIGAN, K., RYAN, K. & SHEARD, G. J. 2006 Wake transition of two-dimensional cylinders and axisymmetric bluff bodies. *J. Fluid Struct.* **22**, 793–806.

THOMPSON, M. C., LEWEKE, T. & WILLIAMSON, C. H. K. 2001 The physical mechanism of transition in bluff body wakes. *J. Fluid Struct.* **15**, 607–616.

TÜRK, S., DASCHIEL, G., STROH, A., HASEGAWA, Y. & FROHNAPFEL, B. 2014 Turbulent flow over superhydrophobic surfaces with streamwise grooves. *J. Fluid Mech.* **747**, 186–217.

WELSH, M. C., HOURIGAN, K., WELCH, L. W., DOWNIE, R. J., THOMPSON, M. C. & STOKES, A. N. 1990 Acoustics and experimental methods: the influence of sound on flow and heat transfer. *Exp. Therm. Fluid Sci.* **3**, 138–152.

WILLIAMSON, C. H. K. 1988 The existence of two stages in the transition to three-dimensionality of a cylinder wake. *Phys. Fluids* **31**, 3165–3168.

WILLIAMSON, C. H. K. 1996 Vortex dynamics in the cylinder wake. *Annu. Rev. Fluid Mech.* **28**, 477–539.

YANG, D., PETTERSEN, B., ANDERSSON, H. I. & NARASIMHAMURTHY, V. D. 2013 Floquet stability analysis of the wake of an inclined flat plate. *Phys. Fluids* **25**, 094103.

YILDIRIM, I., RINDT, C. C. M. & AA, S. V. 2010 Vortex dynamics in a wire-disturbed cylinder wake. *Phys. Fluids* **22**, 094101.

YOON, D. H., YANG, K. S. & CHOI, C. B. 2010 Flow past a square cylinder with an angle of incidence. *Phys. Fluids* **22**, 043603.

ZHANG, H. Q., FEY, U., NOACK, B. R., KÖNIG, M. & ECKELMANN, H. 1995 On the transition of the cylinder wake. *Phys. Fluids* **7**, 779–794.